J. Fluid Mech. (2004), *vol.* 502, *pp.* 309–333.
DOI: 10.1017/S0022112003007730 Printed in the United Kingdom

The breakup of immiscible fluids in turbulent flows

By C. D. EASTWOOD[1], L. ARMI[2] AND J. C. LASHERAS[3]

[1]Department of Aerospace and Mechanical Engineering, University of Southern California, Los Angeles, CA 90089-1453, USA

[2]Scripps Institution of Oceanography and Department of Mechanical and Aerospace Engineering, University of California, San Diego, La Jolla, CA, 92093-0225, USA

[3]Department of Mechanical and Aerospace Engineering, University of California, San Diego, La Jolla, CA, 92093-0411, USA

(Received 17 June 2003 and in revised form 8 October 2003)

The breakup of immiscible fluid particles in a prototypical turbulent flow has been investigated. Dispersed fluids of varying density, viscosity and interfacial tension with water were injected continuously on the centreline in the fully developed region of a turbulent water jet. Digital image-processing techniques were used to track the particle size distributions as the initial globules of the dispersed fluid were broken into smaller particles and convected downstream in the jet. Particle breakup frequencies were calculated from the evolution of the measured particle size distributions using a simplified version of the Boltzmann equation. The results of these calculations indicate that the breakup frequency of fluid particles at low Weber numbers scales with the passage frequency of the large-scale turbulent features of the flow, approximated as u'/L, where u' is the r.m.s. value of turbulent velocity fluctuations and L is the local integral length scale. High-speed video images corroborate this result. Prior to breakup, dispersed fluid particles with initial diameters within the inertial subrange of the background flow stretch to lengths comparable to the local integral scale. These elongated particles subsequently break owing to capillary effects resulting from differences in the radius of curvature along their length. The breakup time of these particles scales with the capillary time $t_d = \mu_d D/\sigma$, where μ_d is the dispersed fluid viscosity, D is the undeformed particle diameter, and σ is the interfacial tension between the dispersed fluid and water. These results are analogous to the breakup mechanisms observed by several investigators in low-Reynolds-number flows; however, they contradict the classical theory for turbulent particle breakup, which suggests that fragmentation results from isolated interactions with turbulent velocity fluctuations over distances comparable to or smaller than the undeformed dispersed particle diameter.

1. Introduction

Many natural and engineering processes involve the transfer of heat or chemical species between two immiscible fluids. Some examples include gas exchange between the oceans and the atmosphere owing to the entrainment of air by crashing waves (Melville 1996), the evaporation of fuel sprays in internal combustion engines, the cooling of industrial exhaust by water sprays, and the delivery of drugs through

aerosol inhalants. Each of these examples involves the dispersion of immiscible particles, either droplets or bubbles, in a continuous turbulent flow. In all cases, the available surface area at the interfaces separating the two immiscible fluids governs the amount of heat or chemical species exchanged. Therefore, knowledge of the size distribution of the fluid particles is critical to developing accurate predictive models of these processes.

Turbulent particle breakup has been the subject of an ongoing investigation, beginning with the pioneering work of Kolmogorov (1949) and Hinze (1955). Workers in the chemical engineering field have invested a considerable effort developing expressions for the equilibrium particle size distribution achieved by turbulent dispersions in stirred tanks and pipelines (Shinnar 1961; Sleicher 1962; Arai *et al.* 1977; Konno, Arai & Saito 1977; Calabrese, Chang & Dang 1986*a*; Calabrese, Wang & Bryner 1986*b*; Wang & Calabrese 1986; Berkman & Calabrese 1988; Hesketh, Etchells & Russell 1991; and others). Other work has focused on the development of models for particle breakup frequency and daughter particle size distribution that can be used to predict particle size distributions once the turbulent flow conditions are known (Coulaloglou & Tavlarides 1977; Konno *et al.* 1980; Konno, Aoki & Saito 1983; Prince & Blanch 1990; Tsouris & Tavlarides 1994; Luo & Svendsen 1996 and others). More recently, a computational study of sub-Kolmogorov scale particle breakup in stochastic flows has been performed (Cristini *et al.* 2003). A review of many of these models can be found in Lasheras *et al.* (2002).

The vast majority of the investigations of turbulent particle breakup performed over the past half-century have been conducted using turbine agitators, like those commonly found in the chemical engineering industry, or turbulent pipe flows. Although these experiments have provided useful information for specific operating conditions of the given devices, they have failed to produce general insight into the mechanisms of turbulent breakup. The results from experiments conducted in agitated vessels or pipes are difficult to interpret because of the complexity of the flow conditions in each of these devices. In both of these experimental configurations, the turbulence is highly anisotropic and contains regions of high mean shear, either near the turbine blades or near the pipe walls. In the current work, a more controlled and more thoroughly understood turbulent flow was used: an axisymmetric high-Reynolds-number turbulent free jet. This flow contains no solid boundaries, so particle interactions with walls or with an intrusive turbulence generating mechanism (e.g. turbine blades) are eliminated. We will describe the results from a series of experiments designed to investigate the breakup of immiscible fluid particles in this canonical turbulent flow. Dispersed fluids of varying density, viscosity and interfacial tension with water were injected continuously on the centreline in the fully developed region of a turbulent water jet. Digital image-processing techniques were used to track the particle size distributions as the initial globules of the dispersed fluid were broken into smaller particles and convected downstream in the jet. From these measurements, particle breakup frequencies were determined based on a simplified version of the Boltzmann equation.

Our measurements indicate that the breakup frequency of particles with non-negligible density at low Weber number, scales with the passage frequency of the large-scale turbulent features of the flow in a manner that is qualitatively analogous to the breakup mechanisms described in Taylor (1934), Rumscheidt & Mason (1961), Grace (1982), Bentley & Leal (1986*b*), Stone, Bentley & Leal (1986), Stone & Leal (1989*a*, *b*), and others in laminar flows, and Cristini *et al.* (2003) in sub-Kolmogorov scale stochastic flows; however, it is contrary to previous results published for the breakup

of immiscible fluid particles in turbulent conditions, described in Lasheras *et al.* (2002).

This paper is organized as follows. Section 2 contains an outline of the experimental facility and methods used to collect and analyse the data presented, including the characterization of the background turbulent flow, a summary of the dispersed fluids used, and a description and validation of our digital image-processing technique. Section 3 describes how the particle breakup frequency is determined from the experimental data based on the population balance equation. It also describes how we defined the 'largest size class', D_{max}, used to determine breakup frequencies from the particle size distributions generated from the raw data and includes the calculated breakup frequencies for each dispersed fluid using two different definitions of D_{max}. Section 3.1 demonstrates how the calculated breakup times (inverse of the breakup frequency) scale with the dispersed fluid properties. Section 4 demonstrates how the breakup frequency scales with the features of the background turbulent flow and includes a discussion of potential resonant interactions between turbulent velocity fluctuations in the background flow and the shape oscillations of the dispersed fluid particles. Section 5 includes images captured with a high-speed video camera that depict the deformation and fragmentation process. Finally, § 6 relates the present results to those reported previously and discusses potential reasons for the difference in the observed particle breakup mechanism.

2. Experimental facility and methods

The experimental facility, shown in figure 1, consisted of a submerged high-Reynolds-number water jet issuing upward from the bottom of a large acrylic water tank. The tank was open at the top end, permitting water to flow out of the tank into a gutter, thereby minimizing recirculation within the tank. The water jet was produced using a nozzle with a contraction ratio of 250:1 and an exit diameter, D_j, of 3.1 mm. A uniform velocity profile at the nozzle exit was obtained by inserting two perforated plates upstream of the nozzle. In the experiments discussed here, $Re_j = U_0 D_j / \nu_c \sim O(10^4)$, where Re_j is the jet Reynolds number, U_0 is the exit velocity of the nozzle, and ν_c is the kinematic viscosity of water. The jet exit velocities used were in the range $12\ \mathrm{m\,s^{-1}} < U_0 < 17\ \mathrm{m\,s^{-1}}$.

The axisymmetric free turbulent jet has been studied extensively over the last fifty years. Reviews of the flow characteristics found in turbulent jets are given in Hinze (1975), List (1982), Monin & Yaglom (1987), Pope (2000) and others. Detailed experimental investigations of this flow are given in Wygnanski & Fiedler (1969) and Hussein, Capp & George (1994), among others. The mean velocities and turbulence properties of the water jet used in the present experiments were measured in order to verify that the flow conditions in the facility matched the well-known characteristics of a free high-Reynolds-number turbulent jet.

Mean values of the axial component of velocity were measured using a laser-Doppler velocimeter. The jet water supply was seeded with 5 μm hollow glass spheres that have an extremely short momentum response time compared to the large-scale turbulent fluctuations existing in the flow. The results of these measurements are shown in figure 2. Following Hussein *et al.* (1994), the centreline axial component of velocity in a self-similar jet is given by:

$$\frac{U_0}{U_C} = \frac{1}{B_u}\left(\frac{X}{D_j} - \frac{X_0}{D_j}\right), \tag{2.1}$$

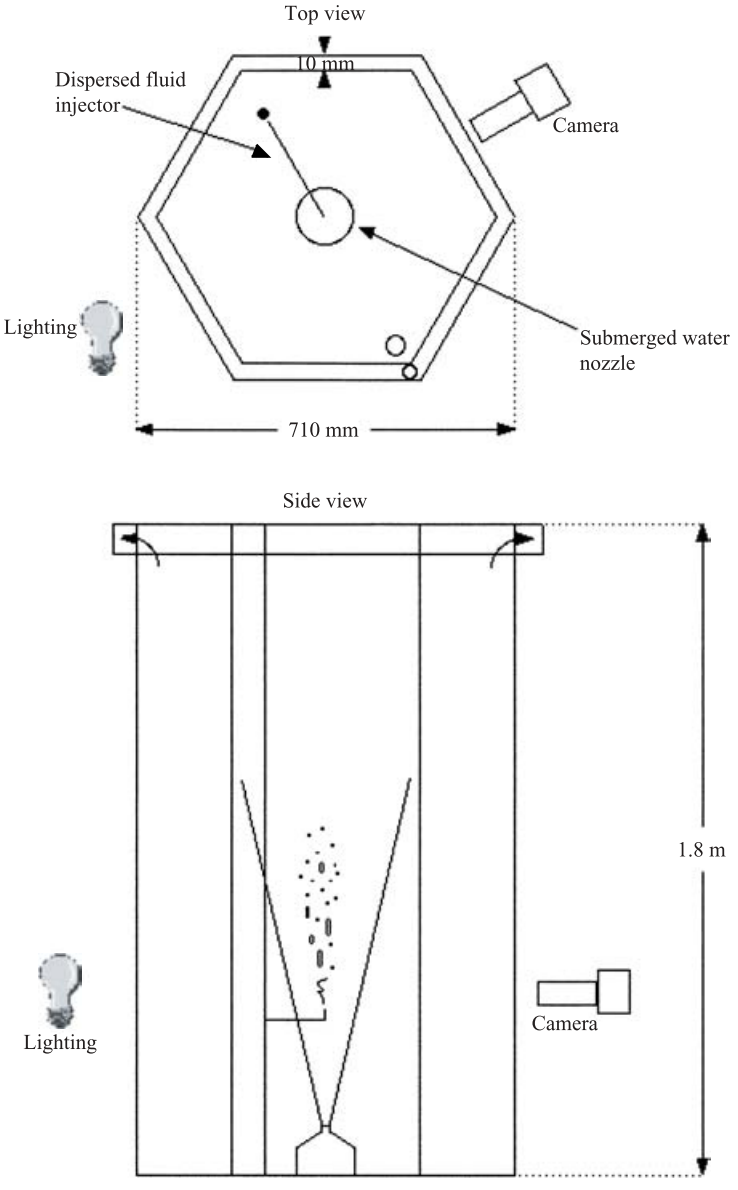

FIGURE 1. Experimental facility.

where D_j is the exit diameter of the nozzle, U_0 is the exit velocity, and U_C is the magnitude of the axial velocity component existing at the centreline at a non-dimensional distance X/D_j downstream in the jet. X_0 is the virtual origin of the jet and B_u is an empirically determined coefficient. The values $X_0/D_j = 3.78$ and $B_u = 4.08$ were determined from these measurements. These values correspond well with those found in Hussein *et al.* (1994) and Wygnanski & Fiedler (1969).

The radial distribution of the axial component of velocity at several downstream locations was determined in Martínez-Bazán (1998) and is shown normalized by the value at the centreline in figure 3. These results are plotted versus the normalized radial distance r/x. It is evident from this figure that the velocity profile becomes

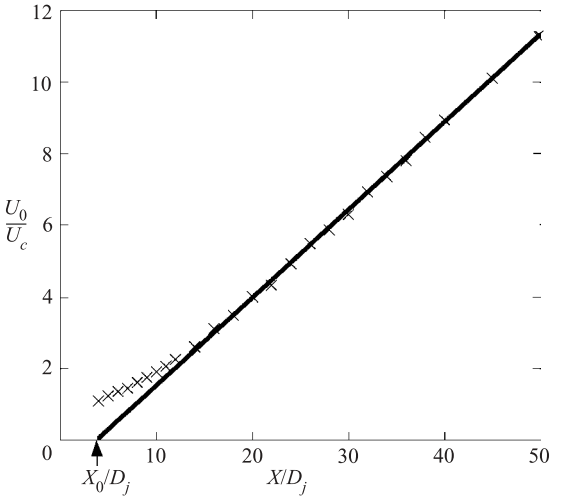

FIGURE 2. Exit velocity, U_0 divided by the centreline value of the axial component of velocity, U_C, measured at successive downstream locations, X/D_j. The x-intercept, $X_0/D_j = 3.78$. $\times$, experimental (LDA) data. —, equation (2.1).

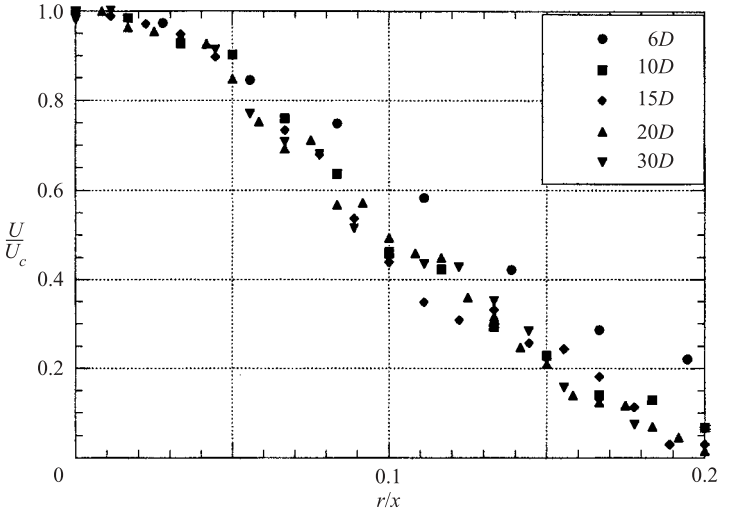

FIGURE 3. Radial distribution of the axial component of velocity. Note that the velocity distribution becomes self-similar after approximately 15 nozzle diameters. [From Martínez-Bazán 1998.]

self-similar at $X/D_j > 15$. In the self-similar region, the axial velocity decays to 90% of its maximum value at $r \approx 0.05x$ and to 50% of its maximum value at $r \approx 0.1x$.

The one-dimensional energy spectrum at the centreline of the jet was obtained using a 1 mm TSI hot-film probe and an A.A. Labs anemometer. Taylor's hypothesis was used to convert the temporal measurements into the spatial domain. The dissipation rate of turbulent kinetic energy, ϵ, was obtained by fitting the following power law, from Hinze (1975), to the region of the spectrum measured at each downstream axial

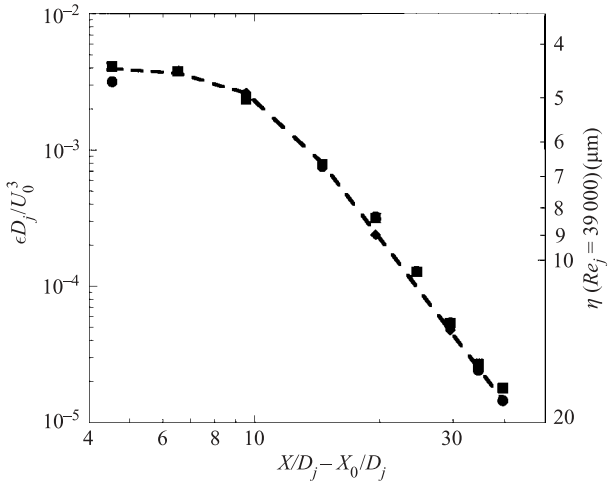

FIGURE 4. Curve-fit for the dissipation rate of turbulent kinetic energy, ϵ, compared with the experimentally determined values. Also shown are the corresponding values of the Kolmogorov length scale, $\eta = (\nu^3\epsilon^{-1})^{1/4}$ for $Re_j = 39\,000$. ●, $U_0 = 17\ \mathrm{m\,s^{-1}}$; ■, $12\ \mathrm{m\,s^{-1}}$; ◆, $13\ \mathrm{m\,s^{-1}}$; – –, fit.

location with $E_1(k_1) \sim k_1^{-5/3}$:

$$E_1(k_1) = \frac{18}{55}\left(\frac{8}{9\alpha}\right)^{2/3}(\epsilon\nu)^{1/4}\left(\frac{k_1}{k_d}\right)^{-5/3}, \tag{2.2}$$

where $E_1(k_1)$ is the one-dimensional energy spectrum, k_1 is the wavenumber corresponding to the axial direction, k_d is the wavenumber corresponding to the Kolmogorov scale, $k_d = (\epsilon/\nu^3)^{1/4}$, ν is the kinematic viscosity of water, and $\alpha = 0.45$ is an empirically determined constant obtained in a high-Reynolds-number turbulent jet by Gibson (1962). The results of these measurements, shown in Eastwood (2002), were in excellent agreement with the values of ϵ determined previously in Martínez-Bazán (1998). The following relation developed in Friehe, Van Atta & Gibson (1971) was used to express the dissipation rate of turbulent kinetic energy as a function of downstream distance in the jet:

$$\frac{\epsilon D_j}{U_0^3} = C\left(\frac{X}{D_j} - \frac{X_0}{D_j}\right)^{-4}, \tag{2.3}$$

where $C = 36$ is an empirically determined constant. In the present experiments, the data was best-fit with a virtual origin $X_0/D_j = 5.47$. This approximation for ϵ is shown in figure 4.

Immiscible fluids of varying viscosity, interfacial tension (with water) and density were continuously injected through a small hypodermic needle located on the centreline of the water jet, in the fully developed turbulent region. The dispersed fluid injector could be positioned at any axial location in the water jet. In the experiments discussed here, the injector needle was placed at an axial location $X/D_j \geqslant 25$, where D_j is the diameter of the water nozzle. Multiple needle diameters could be used to vary the resultant dispersed fluid particle diameter independently of the flow conditions. In all cases, the injection velocity of the dispersed fluid was chosen to match the centreline velocity of the water jet at the injection location. The fluids used as the dispersed phase and their relevant properites are given in table 1. Mass densities

	Density ($kg\,m^{-3}$)	Viscosity (Pa s)	Interfacial tension ($N\,m^{-1}$)
Heptane	684	5.00×10^{-4}	4.8×10^{-2}
Olive oil	881	7.19×10^{-2}	2.0×10^{-2}
10 cSt silicone oil	936	9.7×10^{-3}	3.5×10^{-2}
50 cSt silicone oil	970	5.09×10^{-2}	3.7×10^{-2}

TABLE 1. Dispersed fluid properties.

were measured using a precision mass balance and a volumetric flask. The interfacial tension of each liquid with water was measured using a deNouy-ring tensiometer. The viscosity of each fluid was measured over a range of applied shear rates using a Brookfield viscometer. All fluids tested were Newtonian over the testable range of shear rates. The values of each fluid property determined from these measurements are in close agreement with those found elsewhere in the literature.

Fluid particle sizes were determined using digital image processing. A 500 W incandescent bulb focused through an aspheric condensing lens followed by a symmetric lens was used to provide nearly collimated, uniform backlighting. Images were collected using a Costar CV-M10 digital camera with a shutter speed of 1/80 000 s and a frame rate of 30 f.p.s. The images were captured using a Scion LG-3 frame grabber with a resolution of 640(H) × 480(V) pixels and stored on a hard drive.

For each series of experiments, the camera was focused on an area no greater than 1.9 cm × 1.44 cm, centred on the axis of the water jet. The image resolution was always greater than or equal to 333 pixels cm^{-1}. Four successive downstream camera positions located 1 cm apart were used for each fluid tested. A schematic representation of the measurement conditions is shown in figure 5. At least 3600 images were recorded at each camera location for each test condition. Examples of these images are shown in figure 6. For analysis, each image was divided into five overlapping interrogation windows. Each interrogation window was 18.6 mm wide × 4.5 mm high. It must be emphasized that in all cases, the local width of the water jet was much larger than the width of the interrogation windows (typically, $L_1 \leqslant 0.3 D_{wj}$, where L_1 is the width of the interrogation window and D_{wj} is the local diameter of the water jet). Furthermore, the lateral dispersion of the fluid particles being measured was typically much less than the width of the interrogation window. Therefore, the fluid particles in these experiments were confined to a very small region of the turbulent jet with flow conditions corresponding to the centreline. The assumption of local isotropy has been determined to be valid in this region (Corrsin & Uberoi 1950; Gibson 1962, 1963; Wygnanski & Fiedler 1969; Antonia, Satyaprakash & Hussein 1980; Hussein *et al.* 1994) and the correlation for the dissipation rate of turbulent kinetic energy described above applies.

Fluid particle sizes were obtained by first applying a median filter and then made binary by applying an edge-detection threshold to each image. After thresholding, the area of each fluid particle was determined by counting the pixels comprising that particle. Interior holes, due to the transmission of light through the fluid particles, were included as part of the particle area. Particles that touched the edges of each interrogation window were discarded. The perimeter and projected-area diameter $D = \sqrt{4A/\pi}$, where A is the projected area, were recorded for each particle counted. The perimeter to area ratio was also determined. If this ratio differed dramatically from $4/D$, the corresponding image was visually inspected. If a potential focusing or

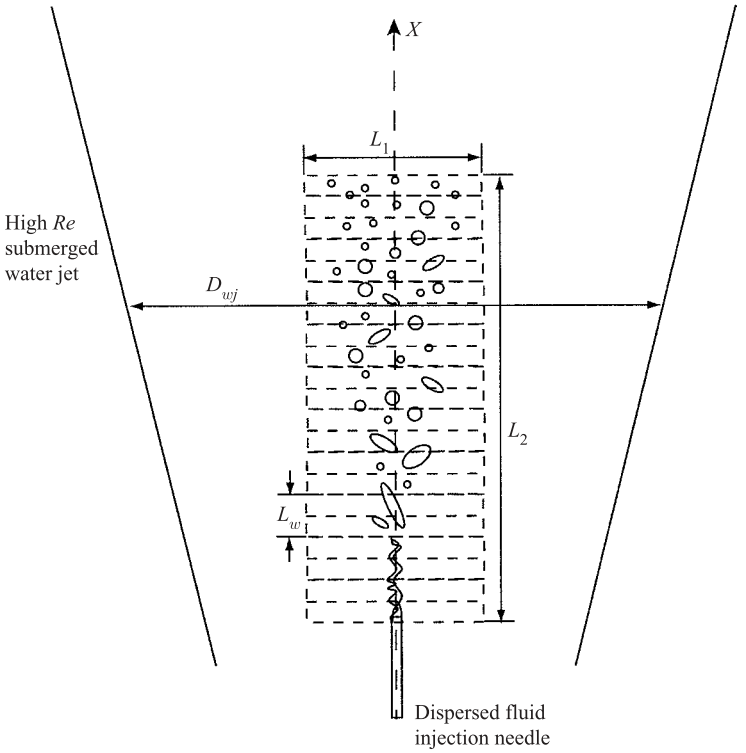

FIGURE 5. Schematic representation of the experimental measurement conditions. Digital images were captured in 20 overlapping interrogation windows located immediately downstream of the dispersed fluid injection point. $L_1 = 18.6\,\text{mm}$, $L_2 = 47.3\,\text{mm}$, $L_w = 4.5\,\text{mm}$. Typically, $L_1 \leqslant 0.3 D_{wj}$.

overlap error was identified, the offending droplet(s) was removed from the data set. Examples of the binary images corresponding to the raw images in figure 6 are shown in figure 7. The particle size distributions obtained for each dispersed fluid using this technique are given in Eastwood (2002).

In order to verify our ability to determine accurately a characteristic dimension for the dispersed particles at each downstream location, the volume flow rate determined from the projected area of the dispersed phase at each interrogation region was compared to the flow rate indicated on the dispersed fluid flow meter (rotameter). It was assumed that the dispersed fluid particles travel at the local mean centreline velocity of the water jet. This was confirmed through laser anemometer measurements for air bubbles in the same facility in Martínez-Bazán (1998); however, it was not confirmed for the current liquid–liquid dispersions. Since the dispersed fluid injection velocity was always chosen to match the local centreline velocity, and since these fluids have densities that are of the same order as water, it is reasonable to assume that they are convected with a mean velocity that matches the local conditions in the water jet. The volume flow rate determined for each fluid is shown in figure 8. The horizontal bands shown in the figure represent $\pm 15\%$ of the flow rate indicated on the dispersed fluid flow meter. The measured volume flow rates for each fluid, indicated by the points on the plot, fall within $\pm 15\%$ of the flow rate indicated on the dispersed fluid flow meter.

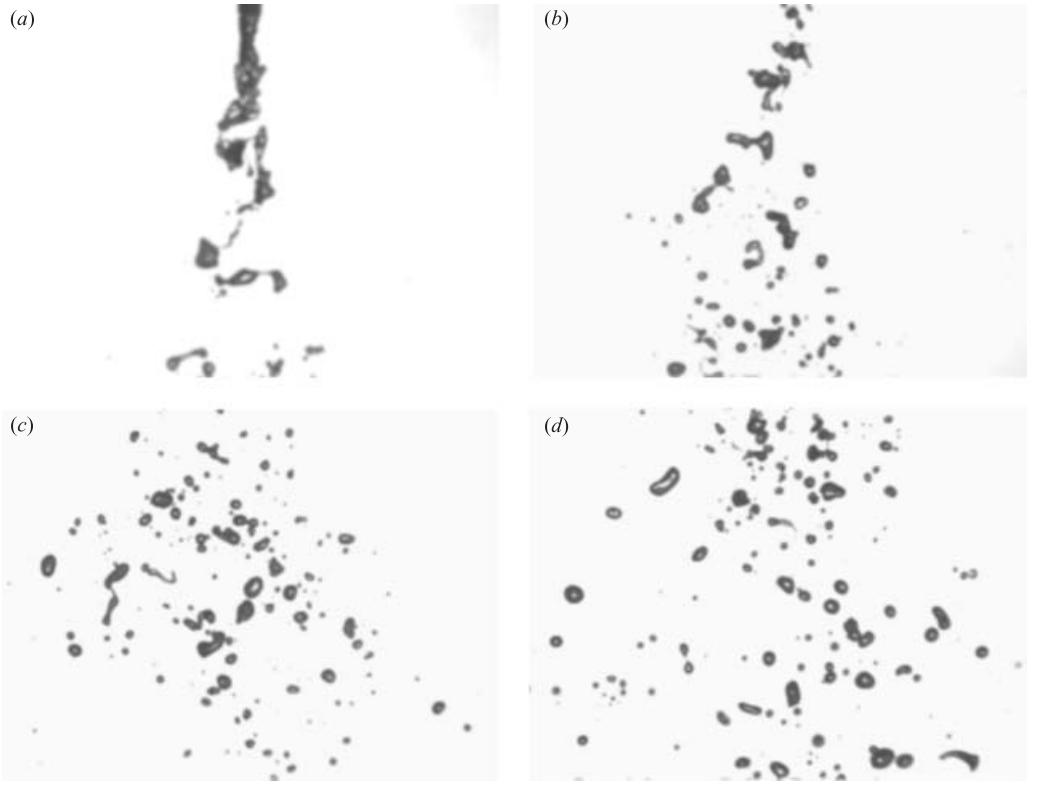

FIGURE 6. Unprocessed images of the breakup of 5 cSt silicone oil injected at $X/D_j = 25$: (*a*) camera position 1, (*b*) camera position 2, (*c*) camera position 3, (*d*) camera position 4. Note that the camera was mounted upside down; therefore, the flow direction in each image is from top-to-bottom.

3. Determination of particle breakup frequency

The breakup frequency of fluid particles can be determined from the population balance equation, as described in Lasheras *et al.* (2002). After integrating over velocity space and in the absence of evaporation or dissolution, the population balance equation becomes (Williams 1985):

$$\frac{\partial n}{\partial t} + \nabla_{\boldsymbol{x}} \cdot (\bar{\boldsymbol{v}}\, n) = \dot{Q}_b + \dot{Q}_c, \tag{3.1}$$

where $n = n(D, \boldsymbol{x}, t)$ is the number density of particles of a given size D at location $\boldsymbol{x}$ at time t, $\bar{\boldsymbol{v}}$ is the mean velocity of these particles, and $\dot{Q}_b$ and $\dot{Q}_c$ are the breakage and coalescence rates, respectively.

If a dispersed system is sufficiently dilute, the probability of particle–particle collisions, and therefore coalescence, is small. In this instance, $\dot{Q}_c$ is small compared to the other terms in equation (3.1) and can be neglected. If, in addition, we consider only the largest particles in a distribution, D_{max}†, then the number of particles of this size cannot change owing to the breakage of larger particles. The population balance

† Our notation D_{max} is not to be confused with the maximum stable, or critical, droplet diameter, defined by Kolmogorov (1949) and Hinze (1955) as $D_{crit} \propto (\sigma \rho_c^{-1})^{3/5} \epsilon^{-2/5}$.

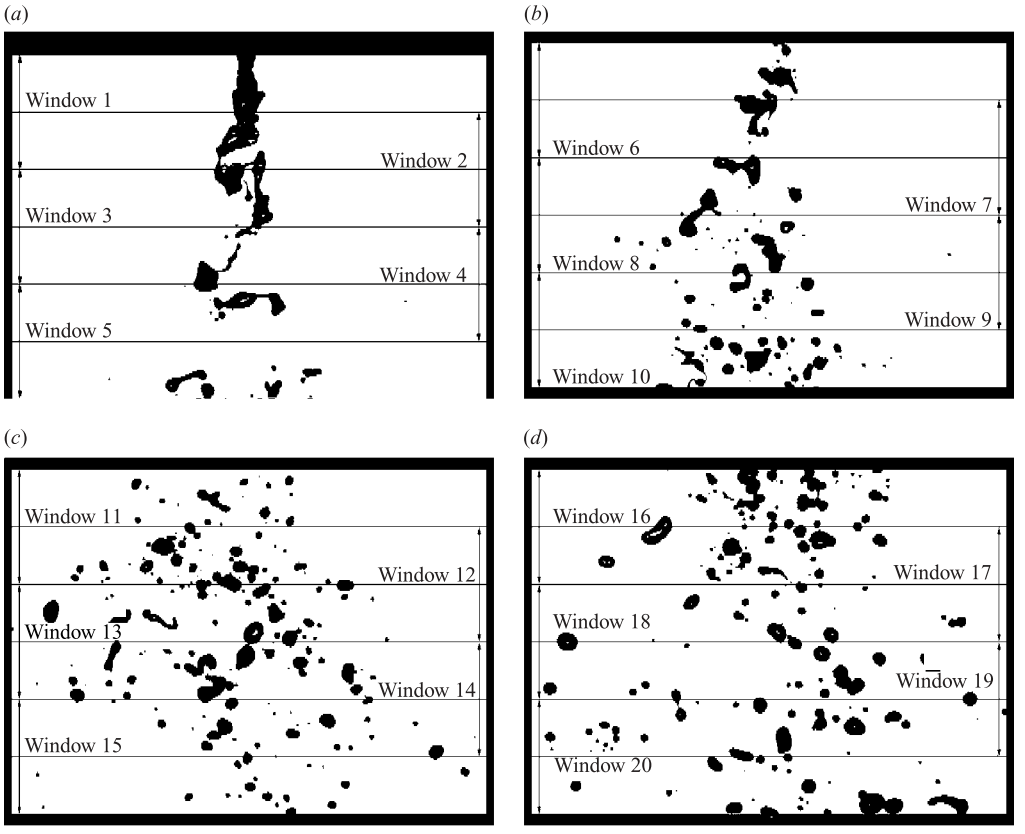

FIGURE 7. Thresholded images of the breakup of 5 cSt silicone oil injected at $X/D_j = 25$. This is the same image sequence as shown in figure 6: (*a*) camera position 1, (*b*) camera position 2, (*c*) camera position 3, (*d*) camera position 4.

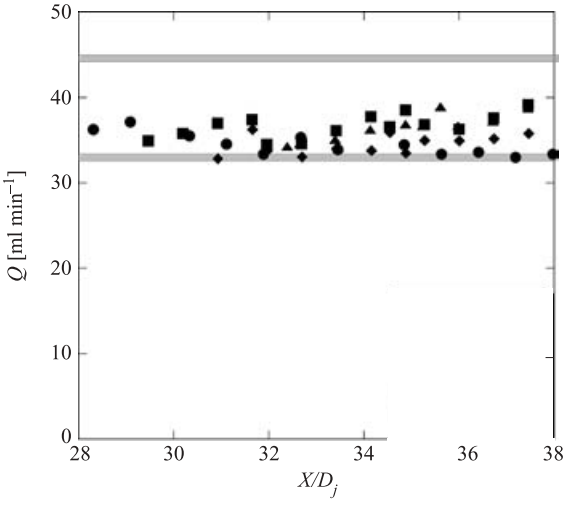

FIGURE 8. Measured volume flow rate versus downstream distance for each fluid tested. ●, heptane; ■, 10 cSt silicone oil; ◆, 50 cSt silicon oil; ▲, olive oil. The horizontal bands indicate ±15% of the dispersed fluid flow meter reading.

equation then simplifies to the following:

$$\frac{\partial n(D_{max})}{\partial t} + \nabla_{\boldsymbol{x}} \cdot [\bar{\boldsymbol{v}}\, n(D_{max})] = -g(D_{max}) n(D_{max}), \tag{3.2}$$

where $g(D_{max})$ is the breakup frequency of the largest diameter particles. For the quasi-one-dimensional steady-state problem under investigation here, this means that the breakup frequency can be determined by examining the flux of particles in the 'largest size class' of each distribution. Since the dimensions of each interrogation window are identical, the number density, $n(D_{max}) = N(D_{max})/(A_w\, L_w)$, where A_w is the cross-sectional area of each interrogation window, can be replaced with $N(D_{max})$, the number of particles in the largest size class. The breakup frequency can therefore be determined from the measured size distributions from the simple expression

$$g(D_{max}) = -\frac{1}{N(D_{max})} \frac{\mathrm{d}}{\mathrm{d}x} [N(D_{max})\, U], \tag{3.3}$$

where, as noted in § 2, U, the local mean velocity of the particles, is taken to be the local mean centreline velocity of the water jet.

Clearly, the determination of particle breakup frequency depends on the definition of the largest size class, D_{max}, that is used. Multiple definitions of D_{max} were employed in order to test the sensitivity to this variable. Plots of $N(D_{max})$ and $N(D_{max})U$ are shown for each fluid tested in figure 9. Two pairs of curves are shown for each dispersed fluid, corresponding to two definitions of the largest size class. For the first pair of curves, the largest size class included particles with diameters greater-than-or-equal-to D_{v80} for the size distribution measured at the first interrogation window. For the second pair of curves, the largest size class included particles with diameters greater-than-or-equal-to D_{v90} at the first interrogation window. Note that D_{v80} is defined as the diameter such that 80% of the total volume recorded corresponds to particles with smaller diameters and D_{v90} is defined such that 90% of the total volume recorded corresponds to particles with smaller diameters. In both cases, the largest size class is fixed by the particle size distribution measured at the first interrogation window and its definition does not change with downstream distance.

Figure 9 indicates that the decay in the number of particles in the largest size class is similar regardless of whether the minimum of the size class is taken as D_{v80} or D_{v90}. The particle breakup frequency was determined by fitting curves to the data shown in these figures and then calculating $g(D_{max})$ according to equation (3.3). These results are shown in figure 10. Notice that the difference between the two curves shown for each dispersed fluid increases with increasing dispersed phase viscosity and/or decreasing interfacial tension between the phases. Since particles with higher viscosity and lower interfacial tension are elongated more significantly prior to breakup, they assume increasingly non-spherical shapes. Furthermore, discrepancies in particle sizing owing to elongation perpendicular to the imaging plane of the camera are likely to be more pronounced for the largest particles in each distribution. The observed differences in the calculated magnitude of the breakup frequency may therefore be the result of inaccuracies in the sizing technique. It is important to note, however, that although the magnitude of the breakup frequency may change significantly with the definition of the largest size class, the dependence of the breakup frequency on X/D_j remains virtually identical in all cases, $g(D_{max}) \sim X/D_j^{-2.1}$.

3.1. *Effect of dispersed fluid properties*

The breakup frequency versus downstream distance obtained for each fluid tested using similar values of D_{max} are shown in figure 11. In each case, $g(D_{max}) \sim X/D_j^{-2.1}$.

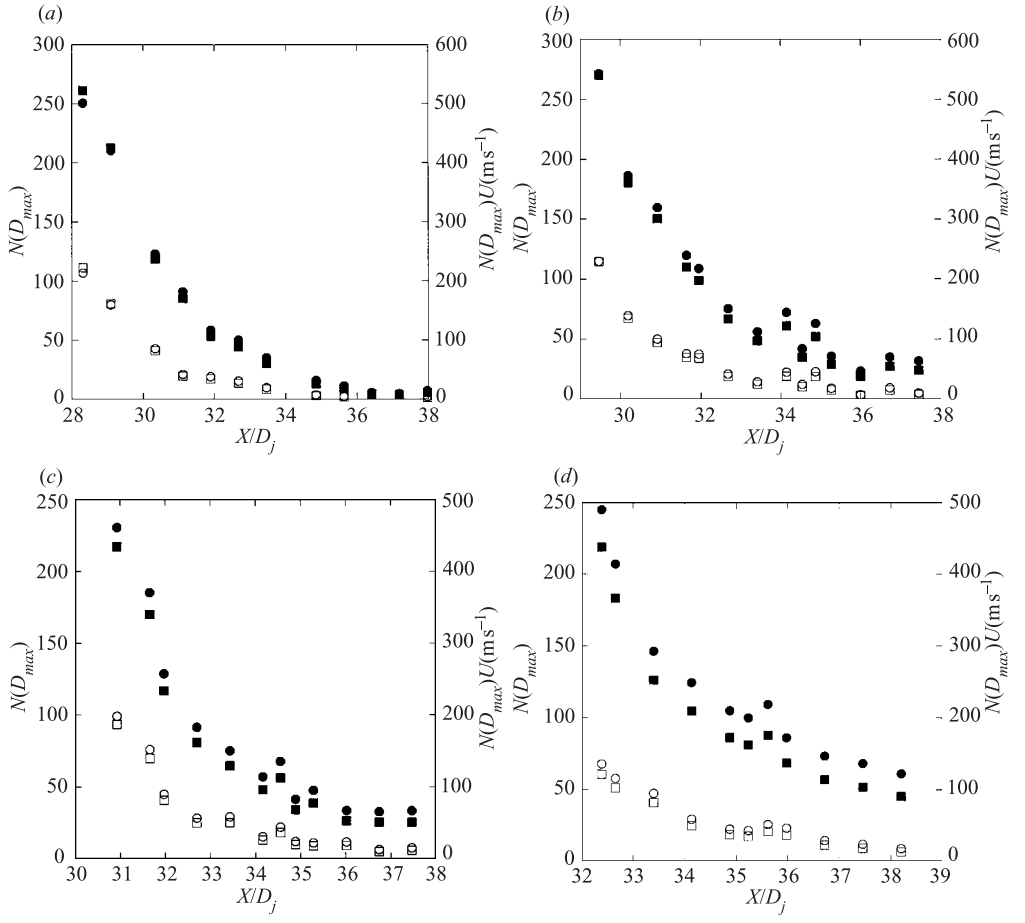

FIGURE 9. Evolution of $N(D_{max})$ and $N(D_{max})U$ with downstream distance for (*a*) heptane, (*b*) 10 cSt silicone oil, (*c*) 50 cSt silicone oil and (*d*) olive oil. ■, $N(D_{max} \geqslant D_{v80})U$; □, $N(D_{max} \geqslant D_{v90})U$; ●, $N(D_{max} \geqslant D_{v80})$ ○, $N(D_{max} \geqslant D_{v90})$.

Note that breakup frequency decreases with increasing viscosity. A time scale can be constructed from the dispersed fluid viscosity, particle size and interfacial tension according to the following:

$$t_d = f(\mu_d, \sigma, D_{max}) = \frac{\mu_d D_{max}}{\sigma}. \tag{3.4}$$

The breakup times, or inverse of the breakup frequencies, corresponding to the values shown in figure 11 at $X/D_j = 35$ are plotted versus this time scale in figure 12. Notice that the calculated breakup frequencies have a linear dependence on t_d.

4. Turbulent scaling

Each of the models for turbulent particle breakup presented in Lasheras *et al.* (2002) follows the classical Kolmogorov–Hinze theory and therefore assumes that particle breakup occurs as the result of a single interaction with a velocity fluctuation over a length that is comparable to the particle diameter. The turbulent stress resulting

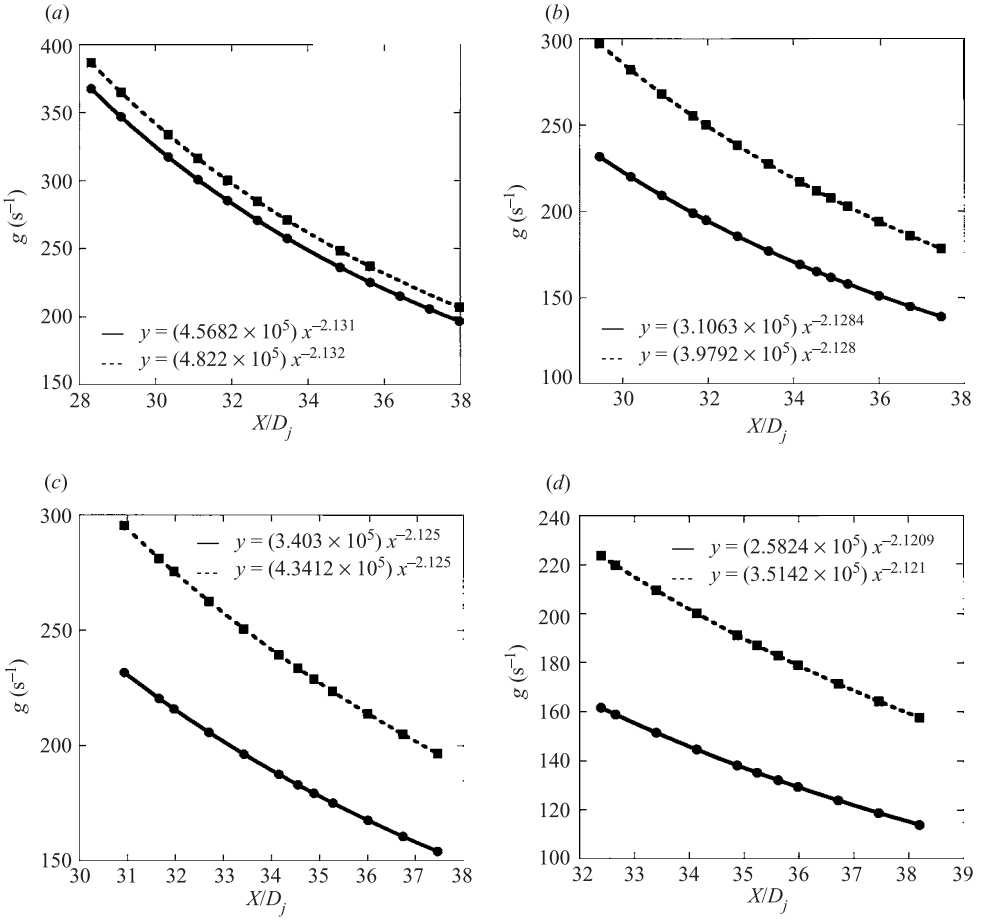

FIGURE 10. Calculated breakup frequency, $g(D_{max})$, versus downstream distance for (*a*) heptane, (*b*) 10 cSt silicone oil, (*c*) 50 cSt silicone oil and (*d*) olive oil. ●, $g(D_{v80})$; ■, $g(D_{v90})$.

from this fluctuation is given by the dynamic pressure:

$$\tau_t(D) = \tfrac{1}{2}\rho_c \overline{\Delta u^2}(D), \tag{4.1}$$

where ρ_c is the continuous phase density and $\overline{\Delta u^2}(D)$ is the mean-squared turbulent velocity fluctuation over a length D. When this stress exceeds the confinement stress due to the interfacial tension, σ, between the particle and the continuous phase, given by

$$\tau_c(D) = \frac{\pi\sigma D^2}{\frac{1}{6}\pi D^3} = 6\frac{\sigma}{D}, \tag{4.2}$$

the particle breaks.

According to Kolmogorov's first similarity hypothesis, given in Kolmogorov (1941*b*), for every turbulent flow with sufficiently high Reynolds number, the statistics of the smallest-scale motions have a universal form that is determined solely by the fluid kinematic viscosity, ν and the dissipation rate of turbulent kinetic energy, ϵ. This smallest scale is known as the Kolmogorov scale and is defined as $\eta = (\nu^3\epsilon^{-1})^{1/4}$. Furthermore, Kolmogorov's second hypothesis states that for every turbulent flow at

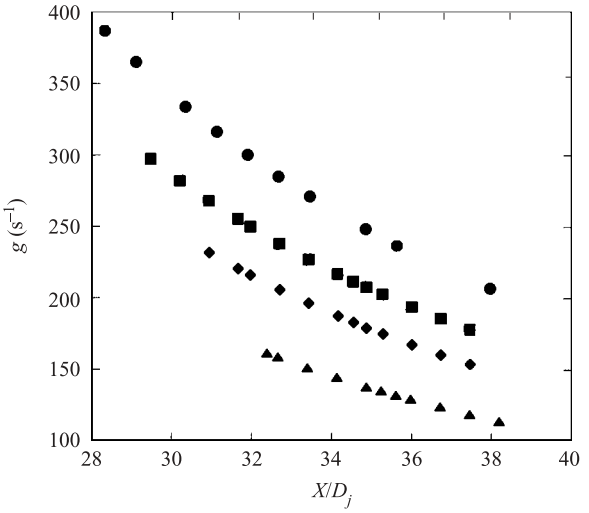

FIGURE 11. Calculated breakup frequency, $g(D_{max})$, versus downstream distance for each fluid tested. Similar values of D_{max} were chosen by adjusting the lower limit of the largest size class between D_{v80} and D_{v90} at the first interrogation window for each fluid. ●, heptane, $D_{max} =$ 1.9 mm; ■, 10 cSt silicone oil, $D_{max} = 1.92$ mm, ◆, 50 cSt silicone oil, $D_{max} = 1.81$ mm; ▲, olive oil, $D_{max} = 1.91$ mm.

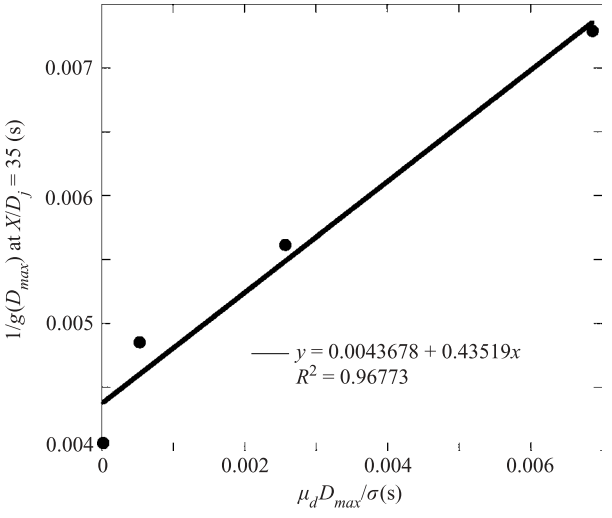

FIGURE 12. The calculated breakup times, or inverse of the breakup frequencies, at $X/D_j = 35$, plotted versus the time scale $t_d = \mu_d D_{max}/\sigma$.

sufficiently high Reynolds number, the statistics of fluctuations of scale l in the range $\eta \ll l \ll L$, where L is the integral scale of turbulent fluctuations, have a universal form that is uniquely determined by ϵ and independent of ν. A turnover frequency for turbulent motions within this range of scales, known as the inertial subrange, can be determined as follows:

$$f_{inertial} = \left(\frac{\epsilon}{l^2}\right)^{1/3}. \tag{4.3}$$

	D_{max} (mm)	Injection location, X/D_j	L_{11}/D_{max}
Heptane	1.92	25	3.2–4.3
10 cSt silicone oil	1.92	25	3.3–4.2
50 cSt silicone oil	1.87	25	3.6–4.4
Olive oil	1.91	25	3.7–4.4
Heptane	1.81	40	5.2–6.4

TABLE 2. Comparison between fluid particle diameters and the local integral scale.

Therefore, if turbulent particle breakup follows the Kolmogorov–Hinze theory, the breakup frequency of fluid particles with diameters in inertial subrange of the turbulent motions in the continuous phase should scale as $g(D_{max}) \sim \epsilon^{1/3}$. This scaling is evident in the model proposed in Martínez-Bazán, Montañes & Lasheras (1999*a*, *b*) and in each of the other models presented in Lasheras *et al.* (2002). In the fully developed region at the centreline of a turbulent jet, $\epsilon \sim (X/D_j)^{-4}$, as indicated previously. Thus, if the Kolmogorov–Hinze theory applies to the breakup observed in the current experiments, the breakup frequency should scale as $g \sim (X/D_j)^{-4/3}$. Figure 10 indicates that the experimentally observed breakup frequency scales as $g \sim (X/D_j)^{-2.1}$. This suggests that the breakup mechanism assumed by the Kolmogorov–Hinze theory does not apply and that an alternative must be developed.

The lateral and longitudinal integral scales, L_{11} and L_{22}, of velocity fluctuations in a turbulent jet scale with $r_{1/2}$, the radius for which the magnitude of the mean velocity is half of its value on the centreline at the same axial location, as discussed in Corrsin & Uberoi (1950), Wygnanski & Fiedler (1969), Friehe *et al.* (1971) and Antonia *et al.* (1980). For the jet facility used in these experiments, $r_{1/2} \approx 0.1x$, as shown in figure 3. The magnitude of velocity fluctuations associated with turbulent features comparable to the integral scale is given by the r.m.s. velocity, u'. The axial r.m.s. velocity fluctuations at the jet centreline were measured in the current facility and were given by $u' \approx 0.25U_c$, where U_c is the centreline velocity. Using the relation for U_c given previously, the strain rate imposed by these large-scale fluctuations scales as

$$s \sim \frac{u'}{L} \sim O\left[\frac{1}{(X/D_j - X_0/D_j)^2}\right], \tag{4.4}$$

where X_0/D_j is the virtual origin. Large-scale strain rates have been estimated at each downstream location using $L_{11} = 0.7r_{1/2}$ following Corrsin & Uberoi (1950), and $u' = 0.25U_c$. The breakup frequencies plotted in figure 11 have been normalized by the local value of the strain rate and are shown versus dimensionless downstream distance, X/D_j in figure 13. This figure clearly demonstrates that for the values of the dissipation rate of turbulent kinetic energy employed, particle breakup for each of the dispersed fluid tested scales with the passage frequency of the large-scale features of the background flow, in contrast with the Kolmogorov–Hinze theory.

Table 2 shows the range of the ratio of the local longitudinal integral scale, L_{11}, to the particle size, D_{max} for each data set shown in figures 11–13. Note that for the dispersed fluids injected at $X/D_j = 25$, the resulting fluid particles are 3.2–4.4 times smaller than the integral scale. An additional experiment was performed by injecting heptane on the jet centreline at $X/D_j = 40$ with a jet Reynolds number of 52 000. This experiment is shown in the last row of the table. The breakup frequencies calculated

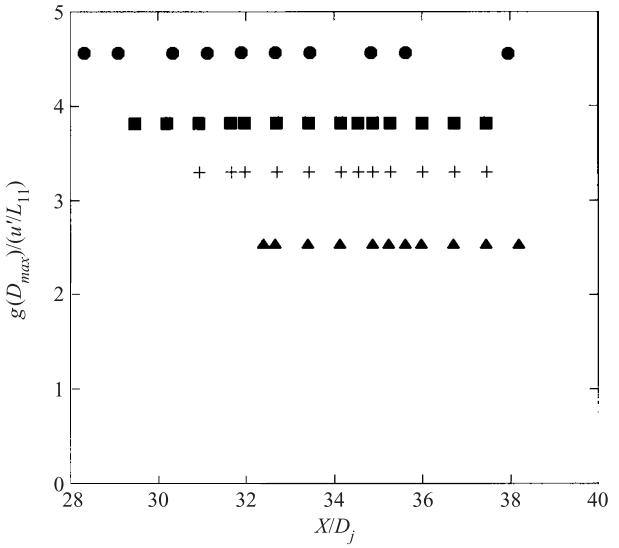

FIGURE 13. Calculated breakup frequencies normalized by u'/L_{11} versus downstream distance. ●, heptane; ■, 10 cSt silicone oil; +, 20 cSt silicone oil; ▲, olive oil.

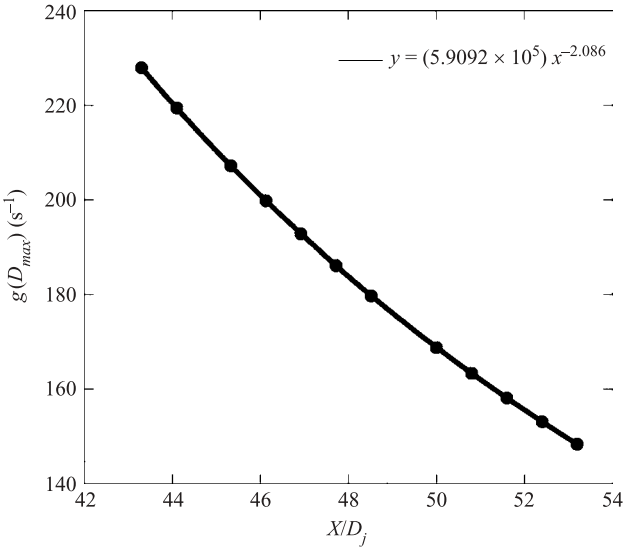

FIGURE 14. Calculated breakup frequency for heptane injected at $X/D_j = 40$. The lower limit of the largest size class was taken to be D_{v90} at the first interrogation window. $D_{max} = 1.81$ mm.

for this experiment are shown in figure 14. Note that even though these particles are an order of magnitude smaller than the local longitudinal integral scale, their calculated breakup frequency scales as $g(D_{max}) \sim X/D_j^{-2.1}$.

Sevik & Park (1973) proposed an alternative mechanism to describe the breakup of air bubbles injected into a turbulent jet; they suggested that particle breakup resulted from a resonant interaction between the natural shape oscillations of the fluid particle and the passage frequency of turbulent structures of similar size. The natural frequency of the nth-order shape oscillation of a spherical particle of diameter

	D_{max} (mm)	Resonance time, $1/f_2$ (s)	Damping time, ζ (s)
Heptane	1.92	1.11×10^{-2}	6.30×10^{-2}
10 cSt silicone oil	1.92	1.41×10^{-2}	1.77×10^{-2}
50 cSt silicone oil	1.87	1.34×10^{-2}	3.33×10^{-3}
Olive oil	1.91	1.82×10^{-2}	2.24×10^{-3}

TABLE 3. Resonance and damping times.

D is given by Lamb (1932) as

$$f_n = \sqrt{\frac{2n(n+1)(n-1)(n+2)\sigma}{\pi^2[(n+1)\rho_d + n\rho_c]D^3}}. \tag{4.5}$$

The most important mode of oscillation is the fundamental mode, corresponding to $n = 2$. The viscosity of the dispersed and continuous phases act to damp the shape oscillations. Lamb determined the damping time for the second mode of oscillation to be given by

$$\zeta_c = \frac{D^2}{80\nu_c} \tag{4.6}$$

when the continuous phase viscosity predominates (e.g. air bubbles in water), and by

$$\zeta_d = \frac{D^2}{20\nu_d} \tag{4.7}$$

when the dispersed phase viscosity predominates (e.g. tar droplets in air).

Risso & Fabre (1998) employed the linear oscillator model of Lamb to describe the breakup of air bubbles in a turbulent field. In dimensionless form, the governing equation for this system is given by

$$\frac{\mathrm{d}^2 r^*}{\mathrm{d}t^{*2}} + 2\xi \frac{\mathrm{d}r^*}{\mathrm{d}t^*} + r^* = K' We(t^*), \tag{4.8}$$

where r^* is the dimensionless particle radius, r/D, D is the undeformed bubble diameter, t^* is the dimensionless time, $2\pi f_2 t$, $\xi = 1/2\pi f_2 \zeta$ is the dimensionless damping coefficient, K' is a dimensionless constant, and We is the Weber number, defined as

$$We = \frac{\rho_c u_x^2(t)\Delta(D)}{\sigma}, \tag{4.9}$$

where $\Delta(D)$ is related to the structure function $\overline{\delta u^2(D)}$. By using a time history for turbulent velocity fluctuations obtained from laser-Doppler anemometer measurements in their facility, Risso & Fabre were able to show that in moderately strong turbulence, the interaction of an air bubble with a succession of eddies may lead to the resonant breakup of the bubble.

The resonance times ($1/f_2$) and appropriate damping times ζ for each fluid tested in the current investigation, using the particle diameters corresponding to the data shown in figure 11, are given in Table 3. Note that in all cases, the second-mode resonance time is of the same order as the damping time. Therefore, unlike the air bubbles studied by Risso & Fabre, the shape oscillations for all of these particles will be significantly damped. For 50 cSt silicone oil and olive oil, the damping time is shorter than the resonance time. For these fluids, the unforced shape oscillations of the

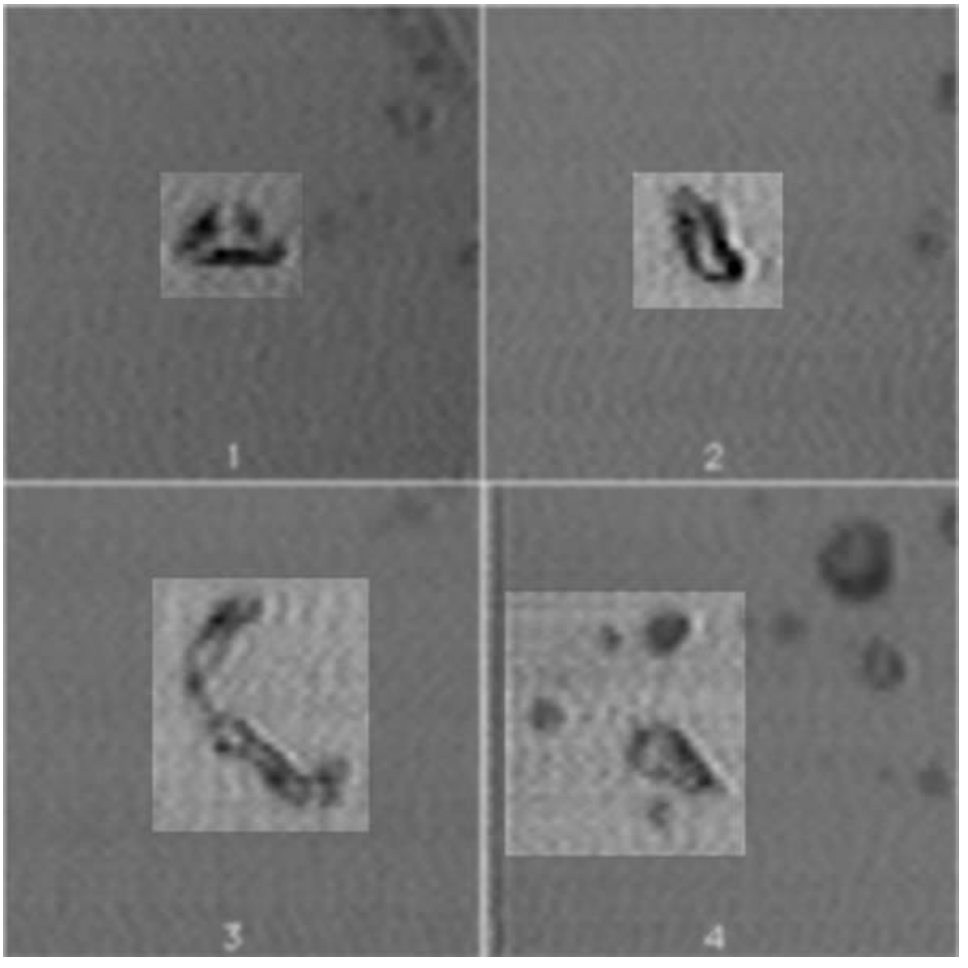

FIGURE 15. High-speed image sequence of the breakup of heptane injected on the centreline of a turbulent water jet. The images are 1/1000 s apart and are located at approximately $X/D_j = 34$.

dispersed particles will be damped appreciably within one oscillation. The total period over which the size distribution of particles in these experiments was recorded was less than $T = 1.4 \times 10^{-2}$ s. This is similar to the resonance times calculated for each fluid. Therefore, even in the absence of damping, resonance cannot be the observed mechanism of particle breakup. Resonant breakup becomes even less plausible if viscous damping effects are included.

5. Deformation and fragmentation

High-speed visualizations of fluid particle deformation and breakup were obtained using a Kodak Ektapro TR1000 high-speed motion analyser and a synchronized strobe light. Typical image sequences are shown for heptane, 10 cSt and 50 cSt silicone oils in figures 15–17. Successive images in each sequence are 1/1000 of a second apart. For these sequences, the dispersed phase was injected at $X/D_j = 30$ and $Re_j = 52\,000$. This yields a mean velocity and dissipation rate of turbulent kinetic energy at the

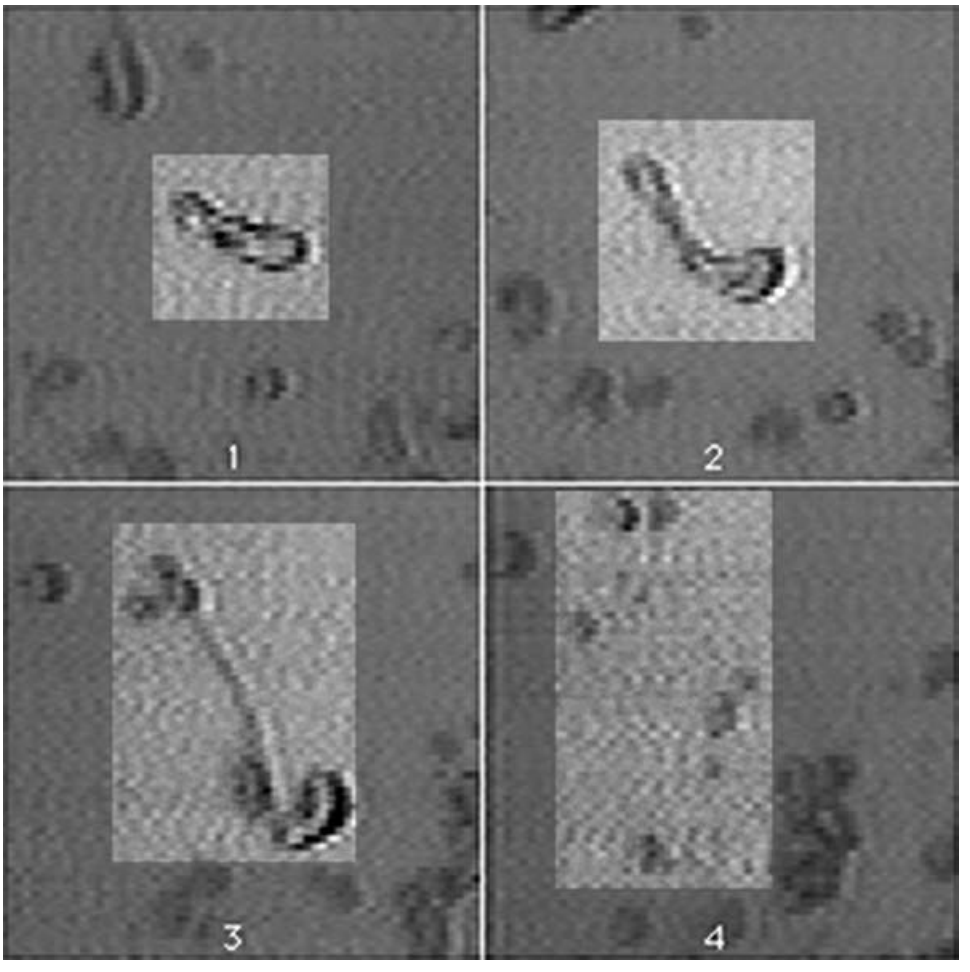

FIGURE 16. High-speed image sequence of the breakup of 10 cSt silicone oil injected on the centreline of a turbulent water jet. The images are 1/1000 s apart and are located at approximately $X/D_j = 35$. It is difficult to identify the daughter particles after breakup in the final image of the sequence.

dispersed fluid injection point that are nearly identical to those obtained at $X/D_j = 25$ with $Re_j = 39\,000$.

The image sequences shown were captured between $X/D_j = 34$ and $X/D_j = 38$, after the initial breakup from the continuously injected column of the dispersed fluid. Notice that in each case, the fluid particles are stretched significantly prior to breakup and that in some cases, particularly the 50 cSt images, they seem to be rotating with the underlying turbulent eddies. breakup, when it eventually occurs, appears to be caused by a capillary-driven mechanism. Fluid tends to accumulate at the ends and sometimes in 'knots' along the length of the elongating particles. breakup occurs at locations where the radius of curvature changes between the thinning region and the bulbous ends or knots. This is analogous to the observations in laminar flows made by Taylor (1934), Bentley & Leal (1986*b*), Stone *et al.* (1986), Stone & Leal (1989*a*), Tjahjadi & Ottino (1991), and others. Estimates of the capillary numbers that apply to the particles shown in the high-speed images ($X/D_j = 35$, $Re_j = 52\,000$)

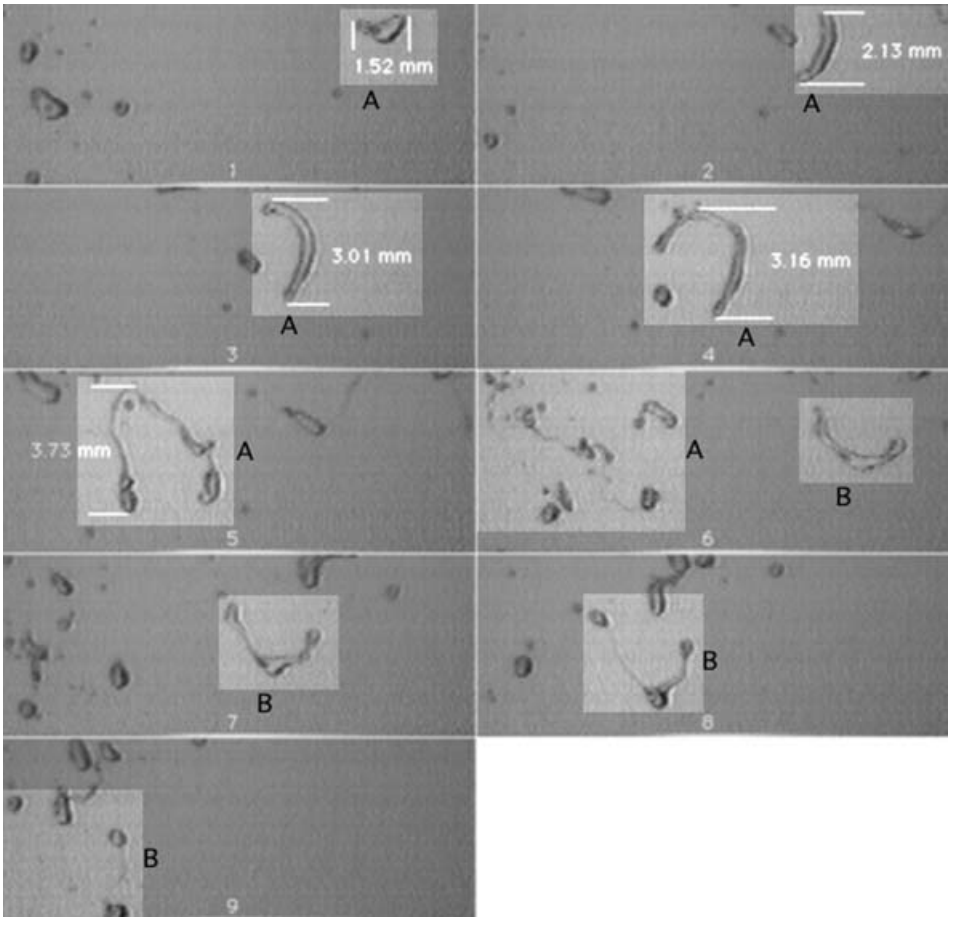

FIGURE 17. High-speed image sequence of the breakup of 50 cSt silicone oil injected on the centreline a turbulent water jet. The images are 1/1000 s apart and are located at approximately $X/D_j = 35$. The deformation and breakup of two particles are shown, labelled as 'A' and 'B'.

	$Re = u'D/\nu_c$	$\lambda = \mu_d/\mu_c$	$Ca = \dfrac{\mu_c(u'/L_{11})D}{\sigma}$
Heptane	1000	0.5	4.3×10^{-4}
10 cSt silicone oil	1000	9.7	5.9×10^{-4}
50 cSt silicone oil	1000	51	5.6×10^{-4}
Olive oil	1000	72	1.0×10^{-3}

TABLE 4. Representative capillary numbers.

are given in table 4. A comparison of these values with the results shown in Janssen & Meijer (1993) indicates that the capillary numbers in the present experiments are approximately three orders of magnitude smaller than the critical values that apply for zero Reynolds number. Notice, however, that the Reynolds number based on particle diameter that applies in the present experiments is approximately 1000. Both Renardy & Cristini (2001*a*, *b*) and Sheth & Pozrikidis (1995) have found that fluid

	$Re_j = \frac{U_0 D_j}{\nu_c}$	$We_t = \frac{2\rho_c(\epsilon D)^{2/3} D}{\sigma}$	$Oh = \frac{\mu_d}{\sqrt{\rho_d \sigma D}}$	$\frac{\rho_d}{\rho_c}$
Heptane	39 000	10	0.002	0.68
10 cSt silicone oil	39 000	20	0.039	0.94
50 cSt silicone oil	39 000	20	0.20	0.97
Olive oil	39 000	30	0.39	0.88
		—Previous study—		
Air	25 500	100	0.001	0.001

TABLE 5. Typical values of the relevant dimensionless parameters for the current experiments and those in Martínez-Bazán (1998) and Martínez-Bazán *et al.* (1999*a*, *b*).

particles will break at subcritical capillary numbers when the Reynolds number is non-zero. Renardy & Cristini showed that the critical capillary number depends on the Reynolds number as $Ca_{crit} = 1/Re_c$. Therefore, it is not surprising that for a Reynolds number of 1000, the Ca_{crit} is three orders of magnitude smaller than the value at $Re = 0$.

The more viscous fluid particles are capable of sustaining greater deformations prior to breakage and can stretch to lengths that are comparable to the large-scale features of the flow. For the 50 cSt sequence, dimensions have been indicated in the first five images. The value of $r_{1/2}$ at the axial location in the turbulent jet where this particle is breaking is approximately 1 cm. Notice that this fluid particle, initially about 1.5 mm in diameter, stretches to a length comparable to $r_{1/2}$ before breakage occurs. The particle seems to be rotating about a length of approximately 3–4 mm, similar in dimension to the local integral scale. Notice that in images 6–9 of the sequence (figure 17), a second particle undergoes a similar elongation and breakup.

Finally, note that resonant shape oscillations are not evident in the breakage sequences. This mode of breakup does not occur, or at least is not prevalent, under these experimental conditions.

6. Discussion

The results presented in this work are in contrast with those obtained previously in the same facility and discussed in Martínez-Bazán *et al.* (1999*a*, *b*) and Lasheras *et al.* (2002). In the previous investigations, the breakup of air bubbles in a turbulent water jet was found to agree with the scaling given by the Kolmogorov–Hinze theory and a model for particle breakup was developed based on a balance between the stress due to turbulent velocity fluctuations over a length comparable to the particle diameter and the confinement stress resulting from the interfacial tension of the particle surface.

A high-speed video sequence of air bubbles breaking at the centreline of a turbulent water jet, taken from Martínez-Bazán (1998), is shown in figure 18. Notice that the bubbles in this sequence assume the 'bulgy'-type deformation described in Hinze (1955). Deformation and fragmentation take place on a scale that is comparable to the original bubble diameter in these images, whereas in the footage shown in the previous section, fluid particles stretch to several times their original diameter before breaking. Clearly, the turbulent breakup mechanism observed in the prior investigation is different from that observed in the current study.

Table 5 compares typical values of the relevant dimensionless parameters in the current investigation to those in the previous study. As mentioned above, the

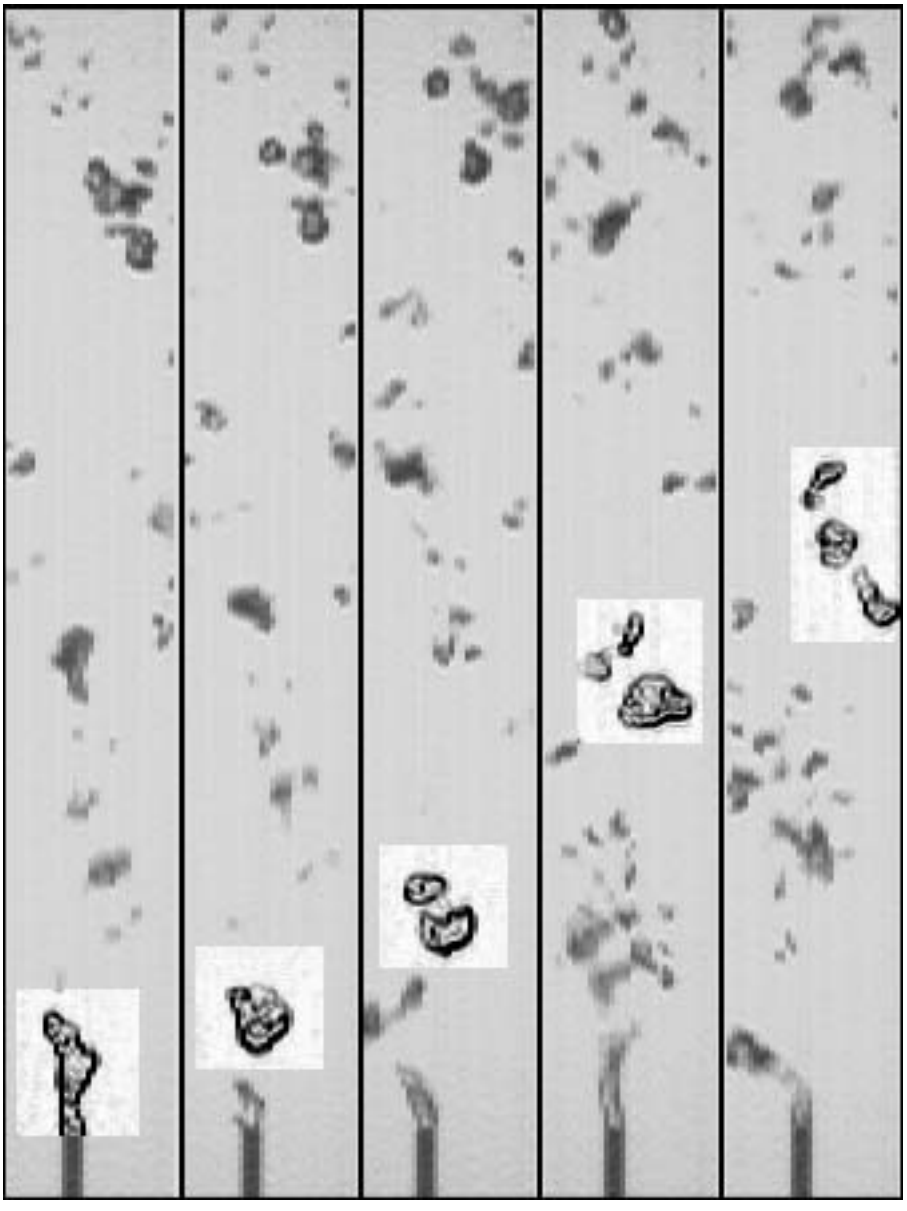

FIGURE 18. High-speed image sequence of the breakup of an air bubble injected on the centreline of a turbulent water jet. The images are 1/6000 s apart and proceed from left to right. The dissipation rate of turbulent kinetic energy at the injection point, ϵ_0, was 1000 W Kg^{-1}. [From Martínez-Bazán (1998)].

Kolmogorov–Hinze theory fits the results of the previous investigation and the predictions of the Martínez-Bazán model match the earlier experimental results. Conversely, the present investigation indicates that for each of the fluids tested, it is more appropriate to scale particle breakup with the large-scale features of the background flow. In the experiments presented in Martínez-Bazán *et al.* (1999*a*, *b*), the dispersed phase was injected further upstream in the turbulent jet in a region with a much greater dissipation rate of turbulent kinetic energy. Note that in the

current investigation, the particle Weber numbers are an order-of-magnitude smaller than those in the previous experiments. Therefore, the excess of energy contained in turbulent scales with dimensions similar to the particle diameter compared to the confining energy due to the interfacial tension of the particles is much smaller in the current investigation than in the previous study. For the less energetic turbulent conditions used here, there may not be enough energy available at lengths comparable to the particle diameter to break the particle in a single interaction, as required by the theory. Interactions with turbulent eddies in the inertial subrange of the background flow may deform the fluid particles but not break them. A succession of interactions might cause the dispersed particles to be deformed sufficiently that they are comparable in length to the large-scale features of the flow. breakup then occurs due to capillary instabilities caused by the strain imposed by the large scales.

7. Conclusions

Existing models for the breakup of fluid particles in a turbulent flow are based on the premise that the structures responsible for breakup are comparable in size to the diameter of the dispersed particles and that breakup is due to the mechanism first proposed by Kolmogorov (1949) and Hinze (1955). A previous comparison between our experimental results for the breakup of air bubbles at the centreline of a turbulent water jet and the predictions of various models for turbulent particle breakup, discussed in Lasheras *et al.* (2002), confirms that this assumption is valid in high-intensity locally isotropic turbulence. For these conditions, we found that the phenomenological model proposed by Martnez-Bazán *et al.* (1999*a*, *b*) accurately predicts the experimental results obtained in our facility. The results of the present study indicate that this model underestimates the experimentally observed particle breakup frequency in the same facility for fluid particles with non-negligible density and viscosity at low Weber numbers. High-speed video images of the breakup of these fluids reveal that the dispersed particles stretch dramatically prior to fragmentation, even within locally isotropic regions of the flow. The amount of stretching observed increases with increasing droplet viscosity. For the most viscous fluids tested, dispersed fluid particles with initial diameters within the inertial subrange or the background turbulent flow stretch to lengths comparable to the local integral scale prior to fragmentation. breakup times at these low Weber numbers scale with the capillary time $t_d = \mu_d D/\sigma$. Furthermore, the calculated breakup frequency (inverse of the breakup time) scales with the large-scale features of the turbulent flow, namely the large-eddy turnover frequency, given by u'/L. These results are analogous to those seen by several investigators in low-Reynolds-number flows; however, they are in disagreement with the classical Kolmogorov–Hinze theory for turbulent particle breakup.

The authors gratefully acknowledge Carlos Martínez-Bazán, J. L. Montañes and Alain Cartellier for their assistance with this work. They also thank the reviewers selected by the editor for their insightful comments and suggestions.

REFERENCES

Antonia, R. A., Satyaprakash, B. R. & Hussein, A. K. M. F. 1980 Measurements of dissipation rate and some other characteristics of turbulent plane and circular jets. *Phys. Fluids* **23**, 695–699.

Arai, K., Konno, M., Matunaga, Y. & Saito, S. 1977 Effect of dispersed-phase viscosity on the maximum stable drop size for breakup in turbulent flow. *J. Chem. Engng Japan* **10**, 325–330.

Bentley, B. J. & Leal, L. G. 1986*a* A computer-controlled four-roll mill for investigations of particle and drop dynamics in two-dimensional linear shear flows. *J. Fluid Mech.* **167**, 219–240.

Bentley, B. J. & Leal, L. G. 1986*b* An experimental investigation of drop deformation and breakup in steady, two-dimensional linear flows. *J. Fluid Mech.* **167**, 241–283.

Berkman, P. D. & Calabrese, R. V. 1988 Dispersion of viscous liquids by turbulent flow in a static mixer. *AIChE J.* **34**, 602–609.

Calabrese, R. V., Chang, T. P. K. & Dang, P. T. 1986*a* Drop breakup in turbulent stirred-tank contactors. Part 1: Effect of dispersed phase viscosity. *AIChE J.* **32**, 657–666.

Calabrese, R. V., Wang, C. Y. & Bryner, N. P. 1986*b* Drop breakup in turbulent stirred-tank contactors. Part 3: Correlations for mean size and drop size distribution. *AIChE J.* **32**, 677–681.

Corrsin, S. & Uberoi, M. S. 1950 Spectrums and diffusion in a round turbulent jet. *NACA TN* 2124.

Coulaloglou, C. A. & Tavlarides, L. L. 1977 Description of interaction processes in agitated liquid–liquid dispersions. *Chem. Engng Sci.* **32**, 1289–1297.

Cristini, V., Blawzdziewicz, J., Lowenberg, M. & Collins, L. R. 2003 Breakup in stochastic Stokes flows: sub-Kolmogorov drops in isotropic turbulence. *J. Fluid Mech.* **492**, 231–250.

Eastwood, C. D. 2002 The breakup of immiscible fluids in turbulent flows. PhD thesis, University of California, San Diego.

Eastwood, C., Cartellier, A. & Lasheras, J. C. 2000 The breakup time of a droplet in a fully-developed turbulent flow. *Proc. Eighth European Turbulence Conf. Barcelona*, pp. 573–576.

Friehe, C. A., Van Atta, C. W. & Gibson, C. H. 1971 Jet turbulence: dissipation rate measurements and correlations. *Turbulent Shear Flows, AGARD Conf. Proc.* **93**, 18-1–18-7.

Gibson, M. M. 1962 Spectra of turbulence at high Reynolds number. *Nature* **195**, 1281–1283.

Gibson, M. M. 1963 Spectra of turbulence in a round jet. *J. Fluid Mech.* **15**, 161–173.

Grace, H. P. 1982 Dispersion phenomena in high viscosity immiscible fluid systems and application of static mixers as dispersion devices in such systems. *Chem. Engng Commun.* **14**, 225–277.

Hesketh, R. P., Etchells, A. W. & Russell, T. W. F. 1991 Bubble breakage in pipeline flow. *Chem. Engng Sci.* **46**, 1–9.

Hinze, J. O. 1955 Fundamentals of the hydrodynamics mechanisms of splitting in dispersion process. *AIChE J.* **1**, 289–295.

Hinze, J. O. 1975 *Turbulence*, 2nd edn. McGraw-Hill.

Hussein, H. J., Capp, S. P. & George, W. K. 1994 Velocity measurements in a high-Reynolds-number, momentum-conserving, axisymmetric, turbulent jet. *J. Fluid Mech.* **258**, 31–75.

Janssen, J. M. H. & Meijer, H. E. H. 1993 Droplet breakup mechanisms: stepwise equilibrium versus transient dispersion. *J. Rheol.* **37**, 597–608.

Kolmogorov, A. N. 1941*a* Dissipation of energy in locally isotropic turbulence. *Dokl. Akad. Nauk. SSSR*, **32**, 19–21.

Kolmogorov, A. N. 1941*b* The local structure of turbulence in an incompressible viscous fluid for very large Reynolds numbers. *Dokl. Akad. Nauk. SSSR*, **30**, 299–303.

Kolmogorov, A. N. 1949 On the breakage of drops in a turbulent flow. *Dokl. Akad. Nauk. SSSR*, **66**, 825–828.

Konno, M., Arai, K. & Saito, S. 1977 The effects of viscous and inertial forces on drop breakup in an agitated tank. *J. Chem. Engng Japan* **10**, 474–477.

Konno, M., Aoki, M. & Saito, S. 1983 Scale effect on breakup process in liquid–liquid agitated tanks. *J. Chem. Engng Japan* **16**, 312–319.

Konno, M., Matsunaga, Y., Arai, K. & Saito, S. 1980 Simulations model for breakup process in an agitated tank. *J. Chem. Engng Japan* **13**, 67–73.

Lamb, H. 1932 *Hydrodynamics*, 6th edn. Cambridge University Press.

Lasheras, J. C., Eastwood, C., Martínez-Bazán, C. & Montañes, J. L. 2002 A review of statistical models for the breakup of an immiscible fluid immersed into a fully-developed turbulent flow. *Intl J. Multiphase Flow* **28**, 247–278.

List, E. J. 1982 Turbulent jets and plumes. *Annu. Rev. Fluid Mech.* **14**, 189–212.

Luo, H. & Svendsen, F. 1996 Theoretical model for drop and bubble breakup in turbulent dispersions. *AIChE J.* **42**, 1225–1233.

Martínez-Bazán, C. 1998 Splitting and dispersion of bubbles by turbulence. PhD thesis, University of California, San Diego.

Martínez-Bazán, C., Montañes, J. L. & Lasheras, J. C. 1999*a* On the breakup of an air bubble injected into a fully developed turbulent flow. Part 1. Breakup frequency. *J. Fluid Mech.* **401**, 157–182.

Martínez-Bazán, C., Montañes, J. L. & Lasheras, J. C. 1999*b* On the breakup of an air bubble injected into a fully developed turbulent flow. Part 2. Size p.d.f. of the resulting daughter bubbles. *J. Fluid Mech.* **401**, 183–207.

Melville, W. K. 1996 The role of surface-wave breaking in air–sea interaction. *Annu. Rev. Fluid Mech.* **18**, 279–321.

Monin, A. S. & Yaglom, A. M. 1987 *Statistical Fluid Mechanics, Mechanics of Turbulence* Vol. 1, 3rd edn. MIT Press, Cambridge, MA.

Pope, S. B. 2000 *Turbulent Flows*. Cambridge University Press.

Prince, M. J. & Blanch, H. W. 1990 Bubble coalescence and breakup in air-sparged bubble columns. *AIChE J.* **36**, 1485–1499.

Renardy, Y. Y. & Cristini, V. 2001*a* Effect of inertia on drop breakup under shear. *Phys Fluids* **13**, 7–13.

Renardy, Y. Y. & Cristini, V. 2001*b* Scaling for fragments produced from drop breakup in shear flow with inertia. *Phys. Fluids* **13**, 2161–2164.

Risso, F. & Fabre, J. 1998 Oscillations and breakup of a bubble immersed in a turbulent field. *J. Fluid Mech.* **372**, 323–355.

Rumscheidt, F. D. & Mason, S. G. 1961 Particle motions in sheared suspensions. XII. Deformation and burst of fluid drops in shear and hyperbolic flows. *J. Colloid Sci.* **16**, 238–261.

Sevik, M. & Park, S. H. 1973 The splitting of drops and bubbles by turbulent fluid flow. *Trans. ASME J. Fluid Engng* **3**, 53–60.

Shinnar, R. 1961 On the behaviour of liquid dispersions in mixing vessels. *J. Fluid Mech.* **10**, 259–275.

Sheth, K. S. & Pozrikidis, C. 1995 Effects of inertia on the deformation of liquid drops in simple shear flow. *Computers Fluids* **24**, 101–119.

Sleicher, C. A. 1962 Maximum stable drop size in turbulent flow. *AIChE J.* **8**, 471–477.

Stone, H. A., Bentley, B. J. & Leal, L. G. 1986 An experimental study of transient effects in the breakup of viscous drops. *J. Fluid Mech.* **173**, 131–158.

Stone, H. A. & Leal, L. G. 1989*a* Relaxation and breakup of an initially extend drop in an otherwise quiescent fluid. *J. Fluid Mech.* **198**, 399–427.

Stone, H. A. & Leal, L. G. 1989*b* The influence of initial deformation on drop breakup in subcritical time-dependent flows at low Reynolds numbers. *J. Fluid Mech.* **206**, 223–263.

Taylor, G. I. 1934 The formation of emulsions in definable fields of flow. *Proc. R. Soc. Lond.* A **146**, 501–523.

Tjahjadi, M. & Ottino, J. M. 1991 Stretching and breakup of droplets in chaotic flows. *J. Fluid Mech.* **232**, 191–219.

Tsouris, C. & Tavlarides, L. L. 1994 Breakage and coalescence models for drops in turbulent dispersions. *AIChE J.* **40**, 395–406.

Wang, C. Y. & Calabrese, R. V. 1986*b* Drop breakup in turbulent stirred-tank contactors. Part 2: Relative influence of viscosity and interfacial tension. *AIChE J.* **32**, 667–676.

Williams, F. A. 1985 *Combustion Theory*, 2nd edn. Benjamin/Cummings, Menlo Park, CA.

Wygnanski, I. & Fiedler, H. 1969 Some measurements in the self-preserving jet. *J. Fluid Mech.* **38**, 577–612.